



LJMU Research Online

Gazak, JZ, Davies, B, Kudritzki, R, Bergemann, M and Plez, B

Quantitative Spectroscopic J-Band Study of Red Supergiants in Perseus Ob-1

<http://researchonline.ljmu.ac.uk/id/eprint/10730/>

Article

Citation (please note it is advisable to refer to the publisher's version if you intend to cite from this work)

**Gazak, JZ, Davies, B, Kudritzki, R, Bergemann, M and Plez, B (2014)
Quantitative Spectroscopic J-Band Study of Red Supergiants in Perseus
Ob-1. *Astrophysical Journal*, 788 (1). ISSN 0004-637X**

LJMU has developed **LJMU Research Online** for users to access the research output of the University more effectively. Copyright © and Moral Rights for the papers on this site are retained by the individual authors and/or other copyright owners. Users may download and/or print one copy of any article(s) in LJMU Research Online to facilitate their private study or for non-commercial research. You may not engage in further distribution of the material or use it for any profit-making activities or any commercial gain.

The version presented here may differ from the published version or from the version of the record. Please see the repository URL above for details on accessing the published version and note that access may require a subscription.

For more information please contact researchonline@ljmu.ac.uk

<http://researchonline.ljmu.ac.uk/>

QUANTITATIVE SPECTROSCOPIC *J*-BAND STUDY OF RED SUPERGIANTS IN PERSEUS OB-1*

J. ZACHARY GAZAK¹, BEN DAVIES², ROLF KUDRITZKI^{1,3}, MARIA BERGEMANN⁴, AND BERTRAND PLEZ⁵

¹ Institute for Astronomy, University of Hawai'i, 2680 Woodlawn Drive, Honolulu, HI 96822, USA

² Astrophysics Research Institute, Liverpool John Moores University, 146 Brownlow Hill, Liverpool L3 5RF, UK

³ University Observatory Munich, Scheinerstr. 1, D-81679 Munich, Germany

⁴ Institute of Astronomy, University of Cambridge, Madingley Road, Cambridge CB3 0HA, UK

⁵ Laboratoire Univers et Particules de Montpellier, Université Montpellier 2, CNRS, F-34095 Montpellier, France

Received 2014 February 3; accepted 2014 April 22; published 2014 May 21

ABSTRACT

We demonstrate how the metallicities of red supergiant (RSG) stars can be measured from quantitative spectroscopy down to resolutions of ≈ 3000 in the *J*-band. We have obtained high resolution spectra on a sample of the RSG population of *h* and χ Persei, a double cluster in the solar neighborhood. We show that careful application of the MARCS model atmospheres returns measurements of *Z* consistent with solar metallicity. Using two grids of synthetic spectra—one in pure LTE and one with non-LTE (NLTE) calculations for the most important diagnostic lines—we measure $Z = +0.04 \pm 0.10$ (LTE) and $Z = -0.04 \pm 0.08$ (NLTE) for the sample of eleven RSGs in the cluster. We degrade the spectral resolution of our observations and find that those values remain consistent down to resolutions of less than $\lambda/\delta\lambda$ of 3000. Using measurements of effective temperatures we compare our results with stellar evolution theory and find good agreement. We construct a synthetic cluster spectrum and find that analyzing this composite spectrum with single-star RSG models returns an accurate metallicity. We conclude that the RSGs make ideal targets in the near infrared for measuring the metallicities of star forming galaxies out to 7–10 Mpc and up to 10 times farther by observing the integrated light of unresolved super star clusters.

Key words: Galaxy: abundances – infrared: stars – open clusters and associations: individual (Perseus OB-1) – stars: abundances – stars: massive – supergiants – techniques: spectroscopic

Online-only material: color figures

1. INTRODUCTION

Measuring metallicities in star-forming galaxies is a ubiquitous goal across the field of extragalactic astronomy. The evolutionary state of a galaxy is imprinted in the central metallicity and radial abundance gradient of iron- and α -group elements. Observed trends in these measurements across ranges of galactic mass, redshift, and environment constrain the theory of galaxy formation and chemical evolution. Central metallicity is dictated by galactic mass, a relationship encoded by the initial properties and evolution of these objects (Lequeux et al. 1979; Tremonti et al. 2004; Maiolino et al. 2008). Radial metallicity gradients provide a wealth of information needed to describe the complex dynamics of galaxy evolution including clustering, merging, infall, galactic winds, star formation history, and initial mass function (Prantzos & Boissier 2000; Garnett 2004; Colavitti et al. 2008; Yin et al. 2009; Sánchez-Blázquez et al. 2009; De Lucia et al. 2004; de Rossi et al. 2007; Finlator & Davé 2008; Brooks et al. 2007; Köppen et al. 2007; Wiersma et al. 2009).

The pursuit of these scientific goals has been undermined by the difficulty of obtaining reliable metallicities. Investigations tend to rely on spectroscopy of the emission lines of H II regions. These methods require empirical calibration and choosing different commonly used calibrations yields varying and sometimes conflicting results from the same set of observations. Both the slope and absolute scaling of metallicity are susceptible to choice of calibration: the mass-metallicity gradient across all galaxies and the radial gradients within individual

galaxies can change from steep to flat while the overall metallicity can shift by a factor of up to four (Kewley & Ellison 2008; Kudritzki et al. 2008; Bresolin et al. 2009). Even the more physical “ T_e -based method” (which utilizes auroral lines to remove the need for “strong line” calibrations) is potentially subject to biases—especially in the metal rich regime characteristic of the disks of all massive spiral galaxies (Bergemann et al. 2014; Stasińska 2005; Bresolin et al. 2005; Ercolano et al. 2010; Zurita & Bresolin 2012).

One technique which avoids the uncertain calibrations of the “strong line” H II region method is the quantitative spectroscopy of supergiant stars. Blue supergiants have become a powerful tool for measuring metallicities, gradients, and distances to galaxies in and beyond the Local Group (WLM—Bresolin et al. 2006; Urbaneja et al. 2008; NGC 3109—Evans et al. 2007; IC1613—Bresolin et al. 2007; M33—U et al. 2009; M81—Kudritzki et al. 2012). This technique, while extremely promising, may also be subject to systematic uncertainties and needs to be checked by independent methods. Moreover, it requires optical spectroscopy. However, next generation telescopes such as the TMT and E-ELT will be optimized for observations at infrared wavelengths, using adaptive optics supported multi object spectrographs. Thus, we need bright abundance tracers which radiate strongly in the IR. Such stars—including red giants, the asymptotic giant branch, and red supergiants (RSGs)—will have a clear advantage in the future.

The extremely luminous RSG stars—which emit 10^5 to $\sim 10^6 L/L_\odot$ largely in the infrared (Humphreys & Davidson 1979)—thus become ideal targets for measuring extragalactic cosmic abundances. Complications due to the densely packed spectral features synonymous with the cool, extended atmospheres of RSGs are minimized in the *J*-band. Here the dominant

* Based in part on data collected at Subaru Telescope, which is operated by the National Astronomical Observatory of Japan.

features are isolated atomic lines of iron, titanium, silicon, and magnesium. Molecular lines of OH, H₂O, CN, and CO manifest weakly or not at all in this bandpass. A new technique proposed by Davies et al. (2010) (henceforth DFK10) has demonstrated that quantitative, medium resolution spectroscopy ($R [\lambda/\delta\lambda] \sim 2000$) in the *J*-band can determine metallicities accurate to ~ 0.15 dex for a single RSG. While a principal limitation of the quantitative spectroscopy of stars is distance, these supergiant studies using 8 m class telescopes have the potential to be extended to ~ 10 Mpc (Evans et al. 2011).

The *J*-band technique is thus poised to study a substantial volume of the local universe, one containing groups and clusters of galaxies. The determination of accurate abundances for the RSG populations of star forming galaxies in this volume will provide an unparalleled observational constraint for models of galaxy formation and evolution. An increased utilization of supergiant stars may also aid in the proper development of the observationally efficient H II-region methods while providing independent alternate measurement technique to the blue supergiants.

Still, DFK10 is a pilot study of the *J*-band technique and the analysis methods to best study these stars requires careful development and testing. Studies of RSGs have classically required high resolutions ($R \sim 20,000$) in the *H*-band in order to separate and study the dense forest of atomic and molecular features present throughout their spectra. Part of this requirement is driven by the scientific desire to study stellar evolution, for which abundances of C, N, and O are important. The *J*-band technique returns no information specific to CNO processing and in exchange avoids the high observational overloads inherent to such studies. This repurposing for extracting global chemical enrichment at modest resolution is novel.

Multiple facets of ongoing research investigate the limitations and systematic uncertainties of the technique in great detail. Davies et al. (2013) provide a thorough investigation of the temperature scale of RSGs in the LMC and SMC and conclude that previous work at optical wavelengths measure effective temperatures which are too cool for these RSGs. They find that MARCS models which fit the strong optical TiO bands produce too little flux in the infrared to fit observed RSG spectral energy distributions. This discrepancy manifests in low measurements of effective temperature when fitting is performed with optical spectroscopy alone. This problem greatly reduced in the near-IR which correspond to deeper atmospheric layers. Additional research is assessing the significance—and observational effects—of the LTE calculations for synthetic spectra produced from the MARCS models. Departures from LTE have been calculated for iron and titanium (Bergemann et al. 2012) and silicon lines (Bergemann et al. 2013) in the *J*-band. Due to the low density environments in the extended atmospheres of RSGs, non-LTE (NLTE) effects are noticeable and can be significant. For this work we have access to synthetic spectra calculated in both LTE (TURBOSPECTRUM—Alvarez & Plez 1998; Plez 2012) and with iron, titanium, and silicon lines in NLTE using the results from Bergemann et al. (2012, 2013).

The aim of this paper is to carefully study the proposed methods of DFK10 and develop a proper understanding of the strengths, limitations, and systematics of the technique. The ideal target for such a study is a nearby coeval population of RSGs in the Galaxy, such that we may study the stars as individual objects and test the potential of utilizing distant super star clusters (SSCs) in which the stellar population becomes an unresolved point source. Theoretical predictions by Gazak et al. (2013) show that in young SSCs the RSG population

dominates the near-infrared flux. In this case the metallicity of the cluster could be extracted by studying the entire cluster as a single RSG. In order to accomplish these goals we target a galactic population of RSGs in the *h* and χ Persei double cluster (henceforth Perseus OB-1) by performing quantitative spectroscopy on high resolution, high precision spectra collected using the Subaru Telescope atop Mauna Kea. The presence of a large population of supergiant stars limits the age of Perseus OB-1 to tens of millions of years, and offers a laboratory for the full range of stellar astrophysics—from IMF to post-main sequence stellar evolution. Currie et al. (2010) present a careful photometric and spectroscopic study of the double cluster and refine the physical parameters of this system. They find an age of 14 ± 1 Myr and estimate a minimum total stellar mass of $20,000 M_{\odot}$. Ages are determined using three methods which return results in good agreement: main sequence turnoff fitting, the luminosities of red supergiants in the clusters, and pre main sequence isochrone fitting. Solar metallicity is a sensible assumption for such a young population in the Milky Way, and studies of the B and A population of supergiant and giant stars—while incomplete—find solar or slightly sub-solar abundances. Our high resolution spectra of eleven RSGs in Perseus OB-1 provide an ideal data set for testing multiple aspects of this project.

This paper is organized as follows. In Section 2 we discuss the observation and reduction of our spectral database. Section 3 contains a description of our atmosphere models and synthetic spectra as well as an outline of the analysis method we have developed. We discuss the results of our fitting in Section 4. We discuss and summarize the results of this work in Section 5.

2. OBSERVATIONS

On the nights of UT 2011 October 4 and 5 we observed 11 of the 21 RSGs in the Perseus OB-1 cluster using the InfraRed Camera and Spectrograph (IRCS; Kobayashi et al. 2000) mounted on the Subaru telescope atop Mauna Kea. The observations took place in non-photometric weather with variable partial cloud cover. We operated to achieve maximum spectral resolution, using the $0'.14$ longslit in echelle mode with natural guide star adaptive optics.

Spectra of targets and telluric standards were bias corrected, flat fielded, extracted and calibrated using standard packages in IRAF. Due to the variable cloud cover each frame was reduced individually and frames overwhelmed by noise were selectively removed. Absolute flux information cannot be recovered in such weather conditions so no flux calibrations were taken or used.

Observations in sub-optimal weather were possible due to the bright apparent magnitudes of the targets, but some spectra suffer from uncorrectable telluric contamination over certain wavelength ranges. For the analysis in this paper we have masked out those spectral regions.

A summary of the observed targets appears in Table 1, with a plot of the high resolution spectra in Figure 1 and a version with the spectra artificially degraded to resolutions of 3000 in Figure 2.

3. ANALYSIS

3.1. Atmospheric Models and Synthetic Spectra

For the analysis of RSGs in our sample we utilize two grids of synthetic spectra calculated using LTE and NLTE radiative transfer. Both grids of model spectra are calculated using as input

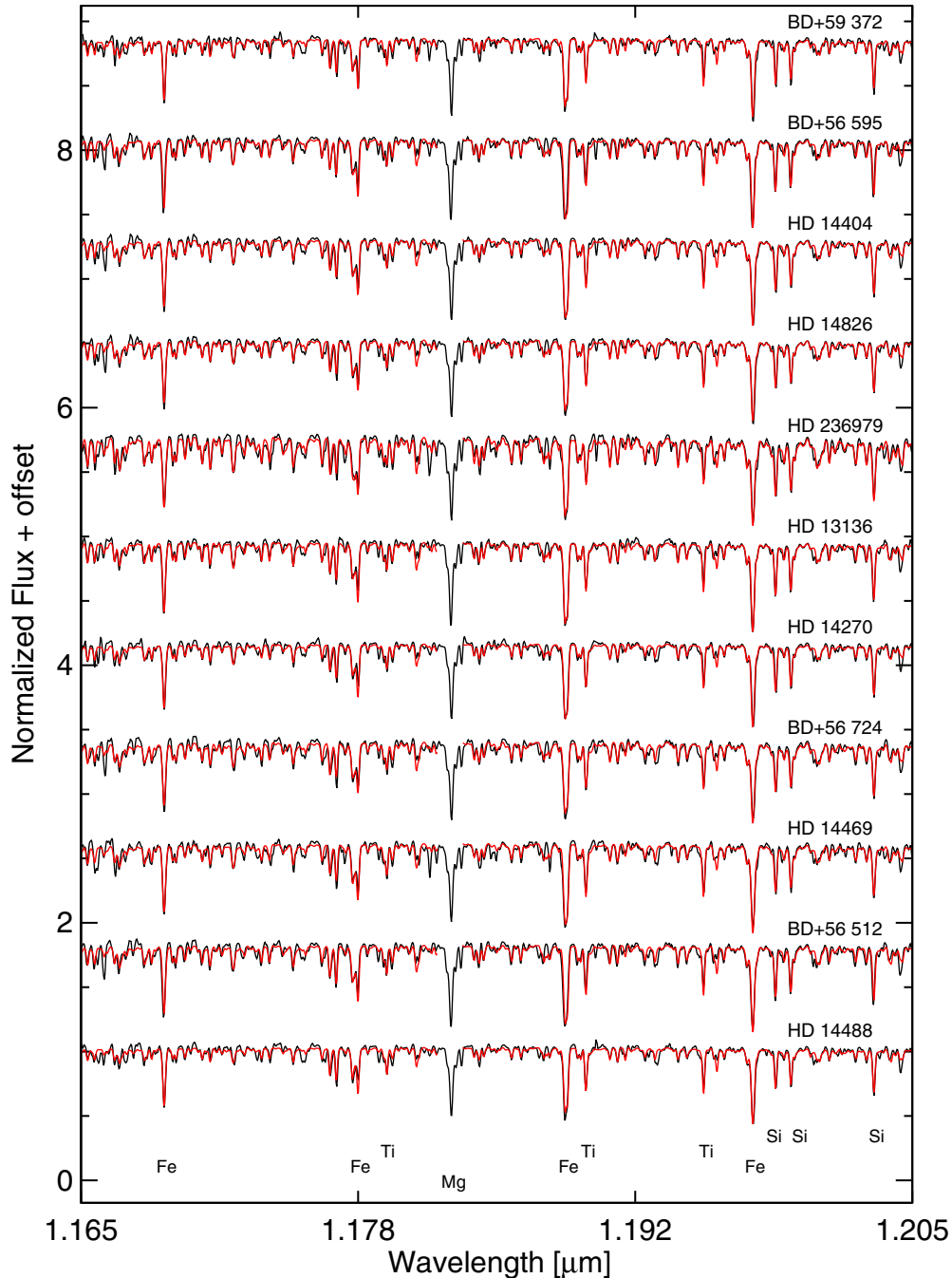


Figure 1. Spectral library of RSGs observed at high resolution with IRCS on Subaru. The main diagnostic atomic lines are labeled. Best fitting NLTE models are over plotted in red. The Mg I line is not included in the fit because it is calculated in LTE but subject to strong NLTE effects. NLTE calculations for Mg I will be implemented soon. Plots are arranged by spectral type (see Table 1).

(A color version of this figure is available in the online journal.)

an underlying grid of MARCS model atmospheres (Gustafsson et al. 2008). These atmospheric models are calculated in one-dimensional (1D) LTE and, while not sharing the complexity of state of the art 3D models, are well suited for this work. Notably, the MARCS model atmospheres have been well tested in the literature and converge quickly such that large grids are possible.

The MARCS grid used in this work covers a four dimensional parameter space including effective temperature, log gravity, metallicity (normalized to Solar values), and microturbulence (T_{eff} , $\log g$, Z , ξ). The dimensions of this grid can be found in Table 2.

The grids of synthetic model spectra used in the analysis of this paper are calculated in first in LTE using TURBOSPECTRUM (Alvarez & Plez 1998; Plez 2012), and second with NLTE diagnostic lines (iron, titanium, and silicon) using the codes developed in Bergemann et al. (2012, 2013). See Figure 3 for a visualization of the effects of the NLTE corrections.

3.2. Continuum Fitting

At high resolutions it is straightforward to scale a model to the continuum level of the data. This is accomplished by selecting the flat regions of the spectrum, performing a polynomial fit

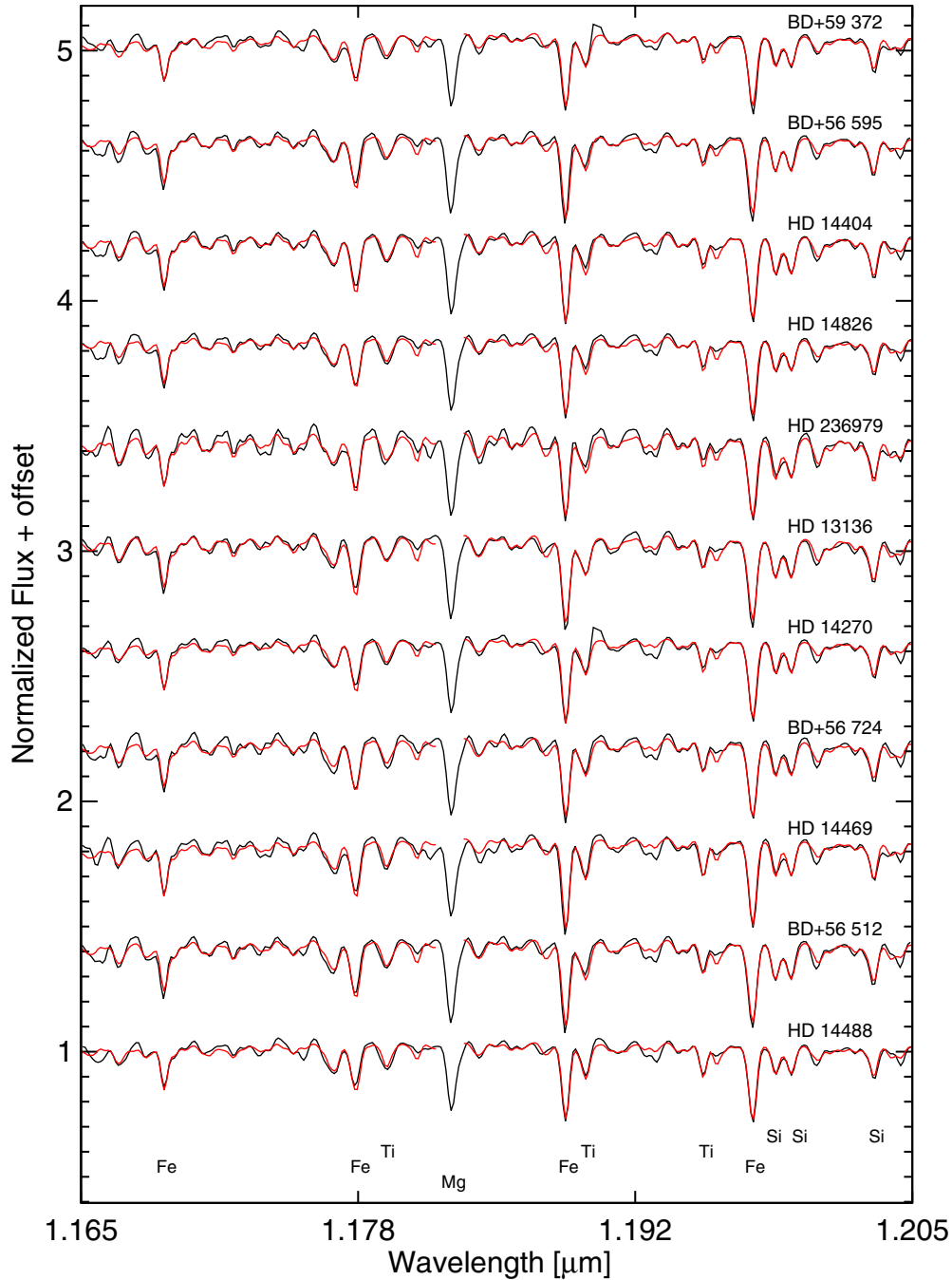


Figure 2. Spectral library from Figure 1 downgraded to a resolution of $R = 3000$. The main diagnostic atomic lines are labeled. Best fitting NLTE models are over plotted in red. The Mg I line is not included in the fit because it is calculated in LTE but subject to strong NLTE effects. NLTE calculations for Mg I will be implemented soon. Plots are arranged by spectral type (see Table 1).

(A color version of this figure is available in the online journal.)

to the ratio of those points to the matching observed flux as a function of wavelength, and then dividing the full wavelength range of the model by this derived fit. In this way we are comparing the depth and shape of spectral features between the observed spectrum and model.

At lower resolutions the effort to correct the continuum increases in complexity as the dense forest of weak molecular lines blend together to form a “pseudocontinuum” such that the entire observation technically lies below continuum level. We illustrate this effect in Figure 4 for $Z = -1.0, 0.0, +0.5$, and $+1.0$ at a spectral resolution of 3000. It is not possible to

know a priori how to then properly correct for the continuum as depth below the true continuum is a function of the stellar parameters themselves, especially metallicity, the primary target of our work.

Our fitting method then becomes a measurement of the ratio of line depth to pseudocontinuum level. We proceed by selecting the points in any given model with normalized flux nearest to unity (see Figure 4, top panel). Assuming this is the continuum we construct an array of the ratio of model to data fluxes at these points. We correct for the continuum by fitting with a low order polynomial and applying that fit to the full model spectrum.

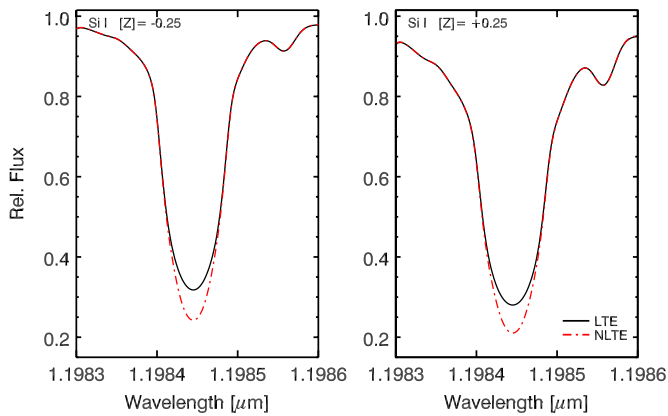


Figure 3. Effects of NLTE corrections on diagnostic lines. Left panel shows a model at $Z = +0.25$, right panel $Z = -0.25$.

(A color version of this figure is available in the online journal.)

Table 1
Perseus OB-1 Red Supergiants

Target	R.A.	decl.	m_V	m_J	m_H	SpT
BD+59 372	01 59 39.66	+60 15 01.9	9.30	5.33	4.20	K5-M0 I ^a
BD+56 595	02 23 11.03	+57 11 58.3	8.18	4.13	3.22	M1 I ^a
HD 14404	02 21 42.41	+57 51 46.1	7.84	3.56	2.68	M1Iab ^b
HD 14826	02 25 21.86	+57 26 14.1	8.24	3.47	2.47	M2 I ^a
HD 236979	02 38 25.42	+57 02 46.2	8.10	3.26	2.30	M2 I ^a
HD 13136	02 10 15.79	+56 33 32.7	7.75	3.00	2.14	M2 Iab ^b
HD 14270	02 20 29.00	+56 59 35.2	7.80	3.38	2.48	M2.5 Iab ^b
BD+56 724	02 50 37.89	+56 59 00.3	8.70	3.10	2.00	M3 Iab ^b
HD 14469	02 22 06.89	+56 36 14.9	7.55	2.82	1.93	M3-4 I ^a
BD+56 512	02 18 53.28	+57 25 16.8	9.20	3.68	2.68	M3 I ^a
HD 14488	02 22 24.30	+57 06 34.4	8.50	3.05	2.11	M4 I ^a

Notes. Target list for calibration of low resolution J -band RSG metallicity extraction. m_V values are adopted from Garmany & Stencel (1992), m_J and m_H from 2MASS (Skrutskie et al. 2006).

^a Spectral type from Levesque et al. (2005).

^b Spectral type from Garmany & Stencel (1992).

Table 2
MARCS Model Grid

Parameter	Notation	Min	Max	Spacing
Eff. Temperature (K)	T_{eff}	3400	4000	100
		4000	4400	200
Log gravity	$\log g$	-0.5	+1.0	0.5
Metallicity (dex)	Z	-1.00	+1.00	0.25
Microturbulence (km s^{-1})	ξ	1.0	6.0	1.0

Note. Parameter grid for MARCS atmospheres (and synthetic spectra) utilized in this work.

In the lower panel of Figure 4 we correct each model to the $Z = 0.0$ model to demonstrate that the models are not degenerate; they remain unique with respect to metallicity even at resolutions suffering the effects of the pseudocontinuum.

3.3. Matching Model Spectra to Data Resolution and Macroturbulence

While a spectrograph disperses incident flux at a characteristic resolution based on grating and slit width, the exact spectral resolution can vary significantly from these expected values based on the size of large-scale turbulent motions, terrestrial atmospheric conditions (e.g., seeing, especially in the case where a point spread function is narrower than the slit width

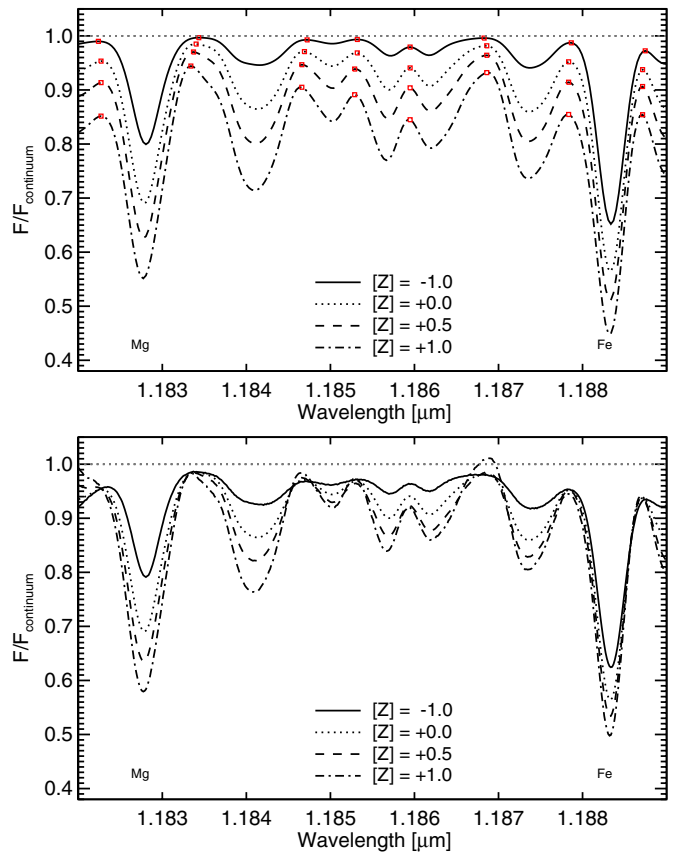


Figure 4. Plot of continuum region between two strong atomic features at spectral resolution of 3000. Each model has $T_{\text{eff}} = 4000$ $\log g = 0.0$, and $\xi = 4.0$. Top panel: models at four values of Z to demonstrate the pseudocontinuum. Red squares mark the continuum points used for each model. Bottom panel: each model is scaled to that of $Z = 0.0$ assuming that it resembles the data set. The variable depth of atomic spectral features as a function of metallicity is still clearly seen. In addition, weak line features strengthen with metallicity and provide additional information with increasing metallicity.

(A color version of this figure is available in the online journal.)

of a spectrograph), and instrument setup (e.g., the focus of the telescope). For these reasons a measurement of spectral resolution is an important component in our analysis.

To accomplish this, each model is degraded to a set of resolutions ranging from twice the expected spectral resolution and down until a χ^2 minimum is passed. We fit a parabola through χ^2 versus resolution. The minimum of this fit is adopted as the best fit resolution for that model. Upon completion we have a set of local minimum χ^2 values each paired with a spectral resolution. We adopt the model with the lowest overall χ^2 as the “best model” and the paired spectral resolution as the proper value for the observed data. At this point we refit the full grid of models locking each at the measured best spectral resolution to calculate a uniform grid of χ^2 values for parameter determination.

The expected resolution of IRCS in our particular setup is R of $\sim 20,000$. We measure resolutions of 11,000 to 14,000 (see Tables 3 and 4). Assuming the difference is caused by macro turbulence, we calculate expected $v_{\text{macro}} \approx 15\text{--}25$ [km s^{-1}]. As the resolution of our observations is on order of 15 [km s^{-1}], we note that these values should serve only as estimates. Still, they are in good agreement with literature values. Ramírez et al. (2000) and Cunha et al. (2007) find RSG macroturbulences

Table 3
Perseus OB-1 Red Supergiants NLTE

Target	T_{eff} (K)	$\log g$	Z (dex)	ξ (km s ⁻¹)	$\frac{\lambda}{\delta\lambda}$ ^a	M/M_{\odot}	Ev. $\log g$	Lit. T_{eff} ^b
BD+59 372	3920 ± 25	+0.5 ± 0.3	-0.07 ± 0.09	3.2 ± 0.2	13600	9.86	+0.72	3825
BD+56 595	4060 ± 25	+0.2 ± 0.7	-0.15 ± 0.13	4.0 ± 0.2	11900	13.2	+0.43	3800
HD 14404	4010 ± 25	+0.2 ± 0.4	-0.07 ± 0.10	3.9 ± 0.2	11100	15.4	+0.24	...
HD 14826	3930 ± 26	+0.1 ± 0.2	-0.08 ± 0.07	3.7 ± 0.4	11200	15.7	+0.18	3625
HD 236979	4080 ± 25	-0.6 ± 0.3	-0.09 ± 0.09	3.1 ± 0.2	11700	16.5	+0.18	3700
HD 13136	4030 ± 25	+0.2 ± 0.4	-0.10 ± 0.08	4.1 ± 0.2	12300	17.7	+0.08	...
HD 14270	3900 ± 25	+0.3 ± 0.3	-0.04 ± 0.09	3.7 ± 0.3	11800	16.2	+0.14	...
BD+56 724	3840 ± 25	-0.4 ± 0.5	+0.08 ± 0.09	3.0 ± 0.2	10900	16.6	-0.05	...
HD 14469	3820 ± 25	-0.1 ± 0.4	-0.03 ± 0.12	4.0 ± 0.2	10200	17.6	-0.17	3575
BD+56 512	4090 ± 35	+0.4 ± 0.3	+0.01 ± 0.12	4.1 ± 0.2	11100	14.7	+0.31	3600
HD 14488	3690 ± 50	+0.0 ± 0.2	+0.12 ± 0.10	2.9 ± 0.2	10500	16.8	-0.07	3550

Notes. Parameter fits to observed RSGs using the grid of synthetic spectra with NLTE corrections to Fe I, Ti I, and Si I lines (Bergemann et al. 2013, 2012). Masses and Evolutionary $\log g$ are calculated using the Geneva stellar evolution tracks which include effects of rotation (Meynet & Maeder 2000).

^a Spectral resolution is measured to ± 100 .

^b Temperatures from Levesque et al. (2005) where target lists overlap.

Table 4
Perseus OB-1 Red Supergiants LTE

Target	T_{eff} (K)	$\log g$	Z (dex)	ξ (km s ⁻¹)	$\frac{\lambda}{\delta\lambda}$
BD+59 372	3930 ± 90	+0.1 ± 0.3	-0.10 ± 0.06	3.4 ± 0.2	13400
BD+56 595	3970 ± 25	+0.2 ± 0.3	-0.08 ± 0.12	4.1 ± 0.2	12400
HD 14404	3950 ± 40	+0.2 ± 0.1	+0.06 ± 0.09	4.1 ± 0.2	11500
HD 14826	3870 ± 25	+0.3 ± 0.2	+0.04 ± 0.10	3.6 ± 0.2	12600
HD 236979	4040 ± 30	-0.5 ± 0.1	+0.01 ± 0.06	3.1 ± 0.2	12300
HD 13136	4030 ± 40	+0.4 ± 0.2	-0.11 ± 0.09	4.3 ± 0.2	12200
HD 14270	3890 ± 25	+0.2 ± 0.3	+0.06 ± 0.12	3.8 ± 0.2	11200
BD+56 724	3740 ± 25	-0.5 ± 0.1	+0.10 ± 0.06	3.2 ± 0.2	11200
HD 14469	3730 ± 25	-0.1 ± 0.3	+0.11 ± 0.13	4.1 ± 0.2	10800
BD+56 512	3940 ± 40	+0.4 ± 0.4	+0.13 ± 0.11	4.1 ± 0.2	11000
HD 14488	3720 ± 70	+0.2 ± 0.1	+0.17 ± 0.08	3.2 ± 0.2	11700

Note. Parameter fits to observed RSGs using the TURBOSPECTRUM grid of synthetic spectra calculated in LTE (Plez 2012; Alvarez & Plez 1998).

of between 11–25 [km s⁻¹] using $R = 40,000$ spectra for a population of galactic RSGs.

3.4. Determination of Stellar Parameters and Errors

After calculating a full four dimensional grid of χ^2 values we extract the best fit parameters. The methodology is as follows. We begin by selecting the “best” model—the model with the lowest χ^2 value. We use the parameters of this model to inform the selection of six two dimensional χ^2 planes (see Figure 5). Functionally, two parameters are locked at the “best values” for each plane and the remaining two parameters are varied against each other. We interpolate the χ^2 grid of each plane onto a parameter grid four times as dense and take the minimum of the dense grid as the best fit values for the two free parameters. After completing this procedure for each of the six planes, we have three measured best values for each parameter. We average these values to arrive at a final fit for each parameter.

We assess the significance of our parameter fits with a Monte Carlo simulation. We begin by constructing a spectrum at the exact extracted parameters by linearly interpolating between points in the model grid. For each of 1000 trials we add random Gaussian noise of strength characteristic of the signal to noise

of the measured spectrum. We fit each noisy interpolated model as described in this section. For each trial we determine the fit parameters and, after completing the computations, analyze the distributions of fitted values for each parameter. In each parameter the zone of $\pm 1\sigma$ is contained between the 15.9 and 84.1 percentile levels. This technique accounts for the noise level in our data as well as any effects based on the spacing in our model grid. We adopt a minimum 1σ value of 20% of the grid spacing for each parameter as we consider a fit more precise than that to be unrealistic given the possibility of nonlinear behavior between grid points. In general our measured significance in metallicity lies above this minimum σ value such that we may confidently trust that our grid is fine enough in metallicity space for this work. In this work we find that lines of Mg I are never well fit. While the cause is under investigation, for this analysis we mask out lines of Mg I before calculating χ^2 .

4. RESULTS

4.1. The RSG Population of h and χ Persei

Initial fits of the spectral database observed for this work measure a slightly sub-solar population metallicity for the Perseus OB-1 RSGs. We measure $Z = +0.04 \pm 0.10$ (LTE) and $Z = -0.04 \pm 0.08$ (NLTE), where the $\pm\sigma$ values denote the standard deviation of the sample. Estimates of the global metallicity of the cluster are more precise, as the error in the mean scales the reported σ 's by $N^{-0.5} = 0.3$ for our population of eleven stars.

The LTE model grid measures higher metallicities for cluster stars than the NLTE grid. This is to be expected; the cores of our strongest diagnostic lines (Fe I, Ti I, and Si I) are deeper in the NLTE case (see Figure 3). For any given observed spectrum, a NLTE fit will provide a lower measurement of metallicity. We find that using a fully LTE grid of MARCS models induces, on average, a shift in Z of +0.07 dex for RSGs near solar metallicity.

We find good agreement between microturbulence values calculated in this work (2.9–4.3 [km s⁻¹] when compared to high resolution spectroscopy ($R \sim 10^5$) of α Ori. Lundqvist & Wahlgren (2005) calculate a value of 4.5 km s⁻¹ using 1D ATLAS9 LTE models. In Wahlgren et al. (2008), the authors refine that value of 3.1 km s⁻¹ after fitting the same data with the newer 1D ATLAS12 LTE models.

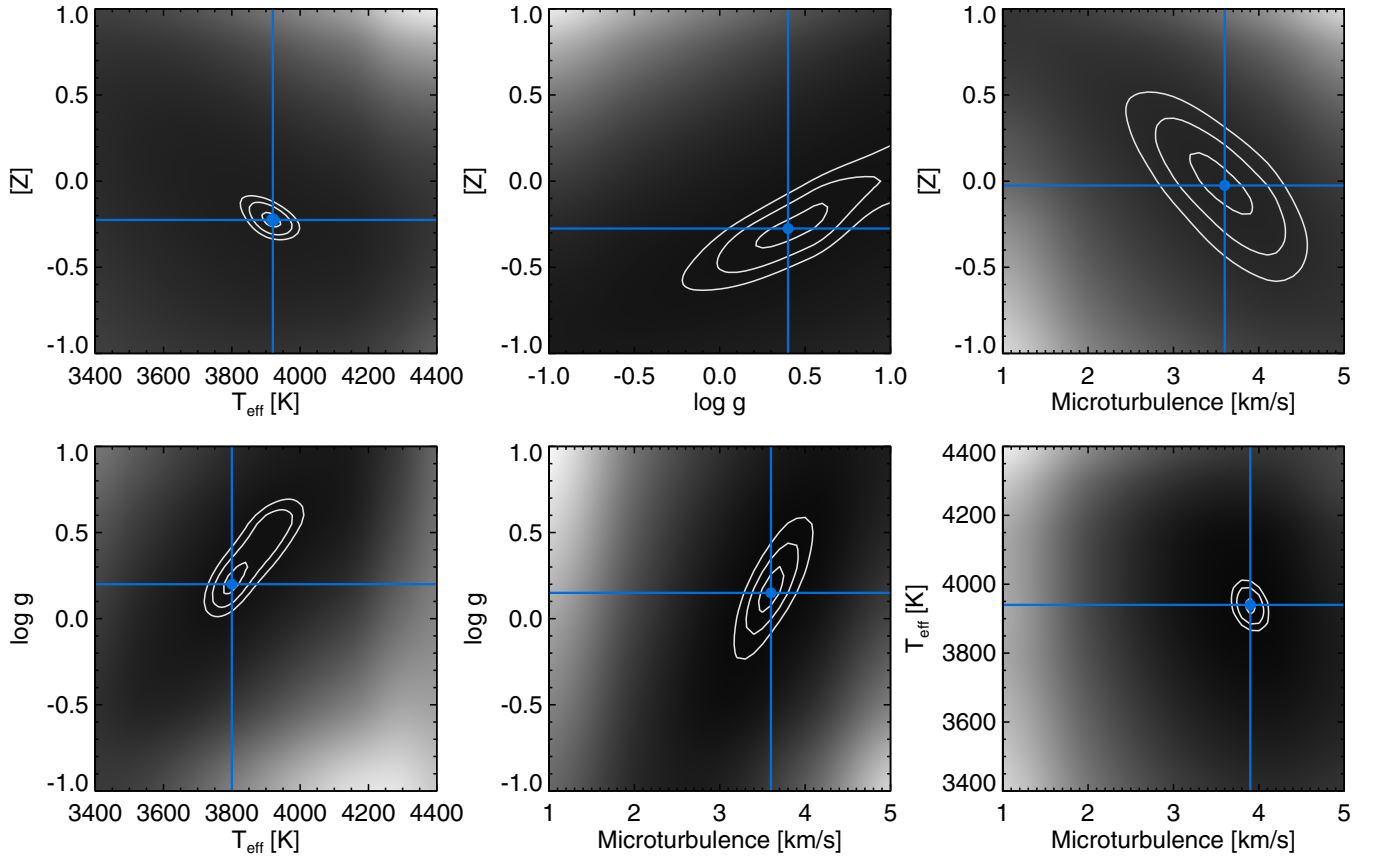


Figure 5. Two-dimensional (2D) contour plots used to extract fit parameters in the analysis procedure. The smooth color gradient is an interpolated χ^2 map, with dark representing lower values (better fits). White contour lines depict fit areas of 1σ , 2σ , and 3σ as determined by Monte Carlo sampling. The blue point at the intersection of blue lines shows the minimum χ^2 in each 2D slice.

(A color version of this figure is available in the online journal.)

4.2. Parameter Stability versus Spectral Resolution

The power of the methodology presented in DFK10 is the need for only moderate resolution of the “new” spectra. In Figure 6 we demonstrate the effect of this degradation for one of our objects. Our high resolution spectral catalogue allows for the first systematic tests of the resolution limits of the *J*-band technique. In the following tests we degrade the resolution of our observed spectra and those spectra become the inputs to our fitting procedure. To achieve this degradation we convolve the high resolution observed spectrum with a Gaussian with characteristic width of $\text{FWHM} = \sqrt{(\lambda/R)^2 - (\lambda/R_{\text{data}})^2}$, where R represents the output resolution of the “new” spectra.

We then follow identically the techniques presented in Section 3, treating each degraded spectra as an independent observation using nothing learned from the actual observations. We iterate from R of 10,000 to 2000 in steps of 1000. At each resolution we calculate the average and standard deviation of measured metallicity for the eleven objects. These values have been plotted in Figure 7. We find that the fitted average metallicity remains stable for both LTE and NLTE grids from spectral resolutions of 12,000 through 2000. Furthermore, the standard deviation in the individual metallicity measurements holds stable at ~ 0.12 dex down to $R = 3000$. At this point individual atomic spectral features become too blended and diluted; the parameter fits of individual objects begin to diverge from high resolution fit values.

We conclude from these tests that the *J*-band technique can be utilized on RSGs down to spectral resolutions of 3000.

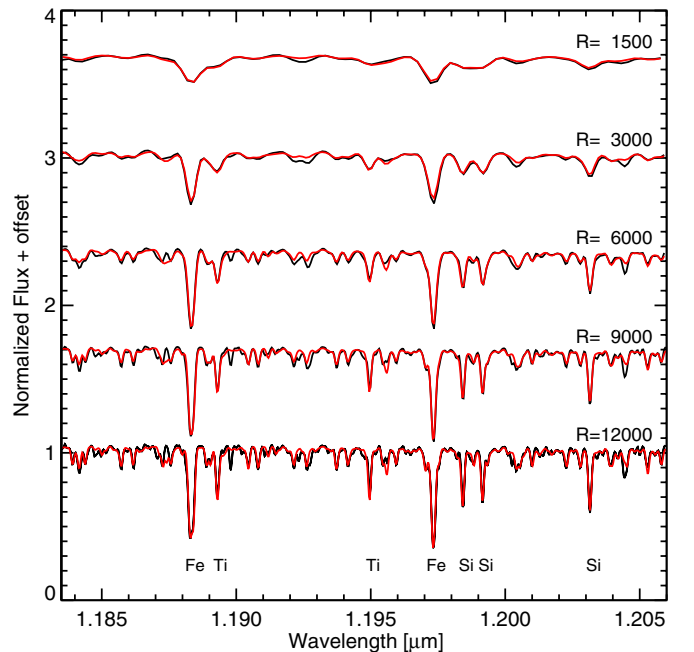


Figure 6. For the analysis in this work we degrade the observed spectra by convolving those spectra with a Gaussian function. The plot shows the effects of spectral degradation on the spectrum of BD+56 595, and each is over plotted in red with the best model spectrum for that data.

(A color version of this figure is available in the online journal.)

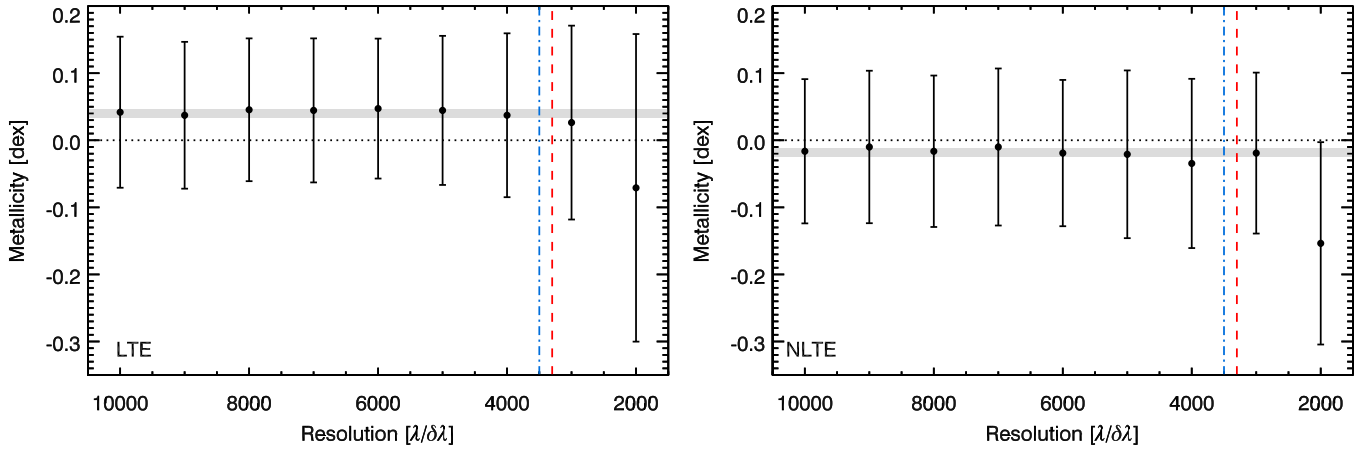


Figure 7. Change in the average measured metallicity for our sample of Perseus OB-1 stars as a function of spectral resolution. Error bars mark the standard deviation of the individual eleven measurements at each step. The horizontal gray region shows $\pm 1\sigma$ of the average metallicity between $12,000 \leq R \leq 3000$, demonstrating the stability of the technique down to resolutions of $R = 3000$. Vertical lines mark the spectral resolutions of key J -band spectrographs, KMOS on VLT in dash-dotted blue and MOSFIRE on Keck in dashed red. A horizontal dotted line marks solar metallicity. We plot results from the LTE model grid (left panel) and NLTE grid (right panel). See Section 3.1 and Section 4.2.

(A color version of this figure is available in the online journal.)

To study large populations of RSGs at extragalactic distances, then, one needs a multi object spectrograph operating at $R \geq 3000$ on a telescope with enough collecting area so that the limiting magnitude is fainter than the target RSGs. Two such instruments exist: MOSFIRE on Keck operates at $R \sim 3200$ and KMOS on the Very Large Telescope (VLT) operates at $R \sim 3400$. These ideal instruments for the study of extragalactic populations of RSGs operate near but safely above the resolution limits of our technique.

4.3. Parameter Stability versus Signal to Noise

In our tests for parameter stability as a function of spectral resolution we assume that at each resolution step we have the same signal-to-noise ratio (S/N) as in the original, high resolution spectrum. This value of S/N is ≈ 100 – 150 per object. By reducing the spectral resolution we functionally increase the S/N per resolution element. In the following, we devise a test to measure the minimum S/N as a function of resolution for which we obtain the same accuracy with respect to metallicity as for our high resolution case.

We calculate the S/N for our original spectra, S/N_{meas} as follows:

$$S/N_{\text{meas}} = \left[\frac{1}{N} \sum_{i=1}^N (F_i - M_i)^2 \right]^{-\frac{1}{2}}. \quad (1)$$

In Equation (1), F is the input spectrum with N points and M is the model in the grid which returns the lowest χ^2 . To measure the required S/N at each resolution we must adjust the effective S/N of the observed spectrum to any S/N_{target} less than S/N_{meas} . This is accomplished by noting that the target S/N is just a quadrature sum of S/N_{meas} and the additional noise spectrum required. The strength of that Gaussian noise, σ_{scale} is then

$$\sigma_{\text{scale}} = \sqrt{S/N_{\text{target}}^{-2} - S/N_{\text{meas}}^{-2}}. \quad (2)$$

Adding random Gaussian noise scaled by σ_{scale} to our observed spectrum degrades it to S/N_{target} .

To understand the S/N necessary to reach our target precision of $\sigma_Z \approx 0.10$ we use the above method starting with a modest

$S/N_{\text{target}} = 5$ and iteratively increase that value until the σ_Z we extract are consistent with those measured for the original spectrum, i.e., any additional S/N provides no increase in fit precision given the data and model grid. The results of this test are plotted in Figure 8, and indicate that for instruments operating at resolutions of ~ 3000 , a S/N of ~ 100 per resolution element is an ideal target for observational programs.

As with our discussion in Section 3.4, we note that the residuals between data and model will not be purely Gaussian in nature. This can be due to any combination of telluric contamination, detector noise, and imperfect model atmospheres. The χ^2_{data} spectrum will contain larger sporadic deviations due to those effects. As a result, the S/N_{meas} of Equation (1) will slightly underestimate the actual S/N of the data. When this propagates into Equation (2), we end up adding too little noise and not quite reaching S/N_{target} . This means that the curve in Figure 8 may be skewed downwards. The amplitude of this effect will vary due to the specifics of each observation. This likely accounts for the scatter present in Figure 8. The overall shift must be small due to the quality of our data and spectral fits. Still, we recommend using the upper limits of the error bars in Figure 8 as a target S/N when planning observations.

We perform a final experiment to test the effects of metallicity on S/N requirements. We interpolate three models from our NLTE grid to values between grid points ($Z = +0.8, 0.0,$ and -0.8) and reanalyze each model as described earlier in this section. The results are plotted in the lower panel of Figure 8. A trend of increasing S/N requirements with decreasing metallicity is indeed seen. The effect is not overwhelming, with less than a factor of two difference between models at $Z = -0.8$ and $+0.8$. The S/N required for this set of spectra are globally lower than the case of the actual data. This is to be expected as the experiment is performed starting with perfect models which show no contamination from non-Gaussian noise sources.

5. DISCUSSION

5.1. Metallicity

The average metallicity of $Z = -0.04 \pm 0.08$ obtained for the Perseus OB-1 RSGs in this work agrees well with the metallicity of young massive stars in the solar neighborhood. Nieva &

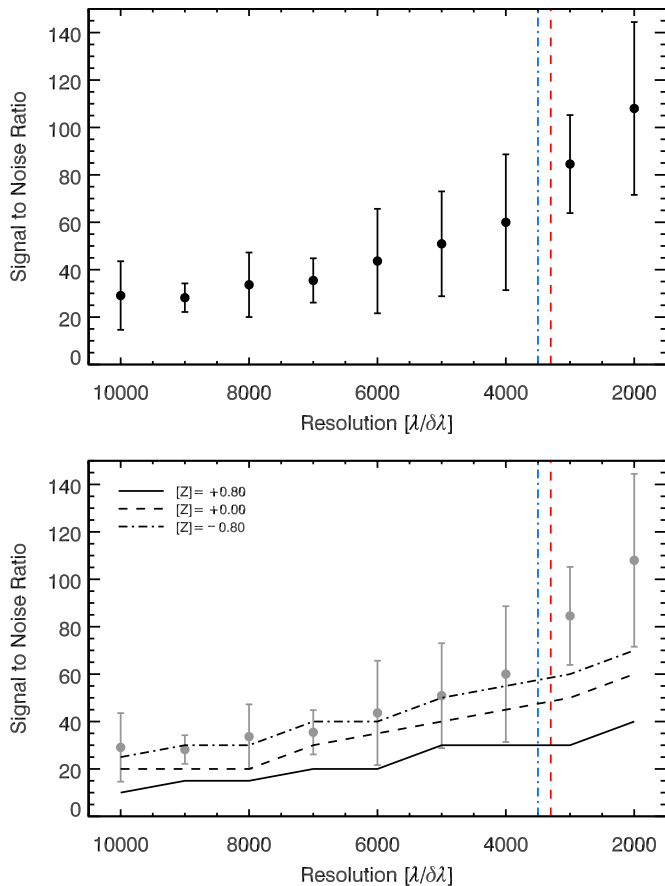


Figure 8. Signal-to-noise ratio needed to achieve target precision for measurement of Z as a function of spectral resolution. Upper panel: each point is the average and standard deviation of the necessary signal to noise ratio for the set of eleven RSG spectra. Lower panel: results for data are grayed out for comparison. Overplotted are signal to noise predictions for models interpolated from the MARCS NLTE grid for metallicities of $+0.8$ (solid), 0.0 (dashed), and -0.8 (dash-dotted). Vertical lines mark the spectral resolutions of key J -band spectrographs, KMOS on VLT in dash-dotted blue and MOSFIRE on Keck in dashed red. For a description of the technique, see Section 4.3.

(A color version of this figure is available in the online journal.)

Przybilla (2012) studied a large sample early B dwarfs and giants using strongly improved detailed NLTE line diagnostics. They obtained surprisingly narrow ($\sigma \approx 0.05$) abundance distributions for the elements C, N, O, Ne, Mg, Si, Fe with average values very close to the sun (Asplund et al. 2009). This implies that there is little scatter in metallicity of the young massive star population around the sun and also practically no chemical evolution over the last 5 Gyr. The fact that we also obtain a metallicity very close to the solar value is, thus, a strong indication that the spectroscopic J -band method leads to reliable results.

Unfortunately, the study by Nieva & Przybilla (2012) does not include objects in Perseus OB-1. However, Firnstein & Przybilla (2012) have recently analyzed A supergiant stars in the solar neighborhood including some objects in Perseus OB-1. While this work does focus on the determination of stellar parameters and does not provide a detailed abundance study, it provides magnesium abundances for three objects with an average value -0.10 dex below the Nieva & Przybilla (2012) average of B stars in the solar neighborhood (the uncertainty for each individual A supergiant is $\approx \pm 0.07$ dex). We take this as a confirmation that the metallicity of Perseus OB-1 is close to solar.

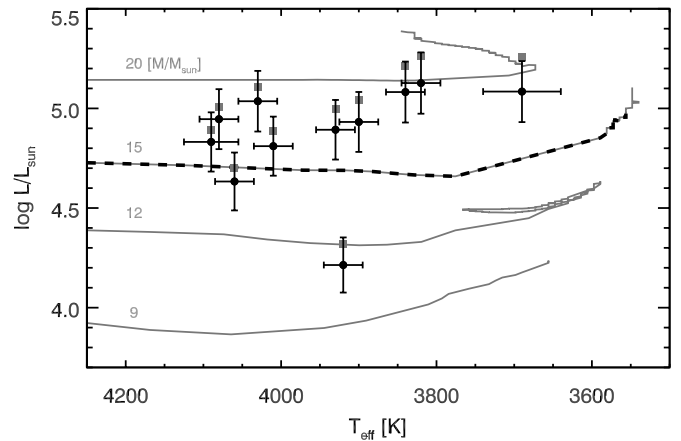


Figure 9. H-R diagram of program stars. Bolometric corrections are taken from Davies et al. (2013). Overplotted in gray are Geneva evolution tracks for solar metallicity including the effects of rotation, labeled with their zero-age main sequence mass. The bold dashed overlay represents the space on the Geneva tracks which covers the literature age of Perseus OB-1, 14 ± 1 Myr (Currie et al. 2010). Gray squares show luminosities calculated using the bolometric corrections of Levesque et al. (2005), which are systematically higher but within 1σ .

5.2. Effective Temperatures

We measure higher T_{eff} for all stars which overlap the target list of (Levesque et al. 2005; see Table 3). The average difference in temperatures is 270 ± 130 [K] for our NLTE calculations (220 ± 100 when compared with our LTE calculations), a significant discrepancy. There are a number of differences between this work and that of Levesque et al. (2005), including the new NLTE corrections we use when computing synthetic spectra, the fact that we fit for Z , micro turbulence, and spectral resolution, and the near IR spectral window of this work. The latter is the most likely candidate for the large difference in measured T_{eff} values. While we work in the J -band, Levesque et al. (2005) use optical spectra, concentrating on the strength of molecular bands of TiO to derive temperatures. Davies et al. (2013) have shown that the derivation of RSG temperatures using quantitative spectroscopy in optical bandpasses returns lower values than are measured using methods which are less dependent on model atmospheres (the *flux integration method*). In addition, Davies et al. (2013) show that optical temperatures over predict the IR flux of RSGs when full spectral energy distributions are available and under predict reddening as compared to nearby stars. Temperatures derived from near IR spectroscopy alone are closer to those values from the flux integration method.

New work with 3D models of RSGs will likely do much to resolve the issue of temperature derivation for RSGs, but only a few of these models are available so far (see, for example, Chiavassa et al. 2011).

5.3. Stellar Evolution

To compare our results with stellar evolution models we first construct an observational Hertzsprung–Russel diagram (HRD). We calculate bolometric luminosities for program stars using archival K band 2MASS photometry (Table 1; Skrutskie et al. 2006), the bolometric correction recipes of Davies et al. (2013) and Levesque et al. (2005), and distance modulus of Currie et al. (2010). We applied the Cardelli et al. (1989) extinction law using measurements of the reddening to Perseus OB-1 (Currie et al. 2010). These luminosities are plotted against the effective temperatures from our spectral fit in the HRD of Figure 9.

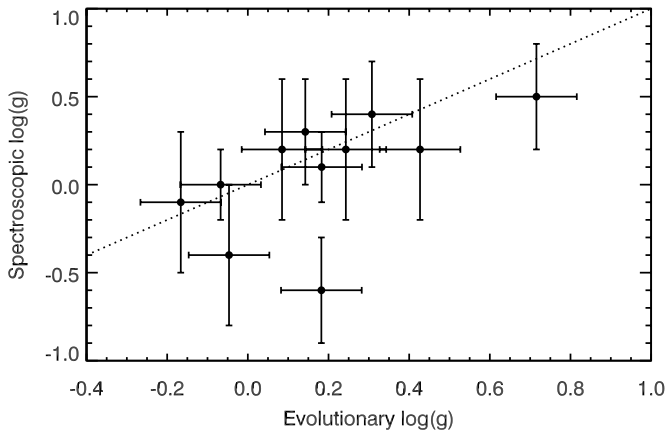


Figure 10. Comparison between parameter fits for $\log g$ and a calculation of the expected $\log g$ values from stellar evolution theory given the age of Perseus OB-1. We find general agreement and note that outliers may be affected by significant turbulent pressure (see Section 5.3).

We then over plot evolutionary tracks adopting the Geneva database of stellar evolutionary models including the effects of rotation (Meynet & Maeder 2000). All stars except one align along the evolutionary tracks, having zero age main sequence masses of $15\text{--}20 M_{\odot}$. This result is in good agreement with the age of Perseus OB-1 of 14 ± 1 Myr (Currie et al. 2010). Only the $15 M_{\odot}$ track agrees with this time frame. At the age of Perseus OB-1, $20 M_{\odot}$ stars have already evolved from the RSG phase while $12 M_{\odot}$ stars are still on the main sequence.

The object BD+59 372 is a clear outlier with a luminosity corresponding to a mass only slightly higher than $9 M_{\odot}$ (see Table 3). At this point we have no explanation for this object.

An independent way to compare our spectroscopic results with stellar evolution is the comparison of gravities $\log g$ obtained from the spectroscopy and from evolutionary tracks. For the latter, we obtain a stellar mass from the observed luminosities by interpolating evolutionary track masses and luminosities at the effective temperature observed. This mass is then used in conjunction with the observed luminosity and effective temperature to calculate evolutionary gravities. Figure 10 compares evolutionary gravities obtained in this way with spectroscopic gravities. Besides one outlier (HD 236979) we find general agreement and no indication of a systematic discrepancy. We also note that the outlier in Figure 9, BD+59 372, as the object with the highest gravities agrees within the uncertainties of the error bars.

The general agreement between spectroscopic and evolutionary gravities can be used to discuss the influence of convective turbulence pressure on the model atmosphere stratification. The 3D-hydrodynamic convection simulations by Chiavassa et al. (2011) include effects of pressure caused by the convective motion on the atmospheric density stratification. On the other hand, the 1D MARCS models used in our analysis do not account for convective pressure. It is straightforward to show (see, for instance, Chiavassa et al. 2011, Equation (8)) that as the result of convective pressure the stellar gravity is reduced to an effective gravity which can be approximated by

$$\log g_{\text{eff}} = \log g - \log \left(1 + \beta v_{\text{turb}}^2 / v_{\text{sound}}^2 \right) \quad (3)$$

where v_{turb} is the average turbulence speed and v_{sound} the sound speed. β is a parameter close to unity if the turbulent velocity fields is almost isotropic. Chiavassa et al. (2011) concluded from their calculations and a comparison with MARCS models

that gravity corrections of 0.25–0.3 dex are needed to match the density stratifications of the 1D with the 3D models corresponding to turbulence velocities of the order of the sound speed.

Our comparison of spectroscopic and evolutionary gravities does not indicate a systematic effect of this order. On the other hand, our two objects with the lowest spectroscopic gravities may well be influenced by large effects of turbulence pressure. We note, however, that the models used to calculate our synthetic spectra and those models used for the stellar evolution calculations of (Meynet & Maeder 2000) utilize 1D models which may affect stellar evolution and atmosphere predictions in the same way.

5.4. Simulation of Super Star Cluster Spectral Analysis

The scientific strength of the low resolution J -band technique derives from the radiative power of RSG stars. In this work we carefully demonstrate that the method is stable and precise well below the spectral resolution of current instrumentation on the largest telescopes available, notably MOSFIRE on Keck and KMOS on the VLT. With these multiplexed instruments we are able to efficiently apply this technique to entire populations of RSGs as individual objects over extragalactic distances. DFK10 calculate a limiting distance for the technique of 7–10 MPC using a single RSG.

In Gazak et al. (2013) we presented simulations showing that the near-IR flux of young SSCs is dominated by their RSG members. These simulations show that the J -band spectrum of a SSC older than 7 Myr will appear very similar to that of a single RSGs. This opens the possibility to use the integrated J -band light of SSCs in distant galaxies as a source for spectroscopic determination of galaxy metallicities.

Our collection of Perseus OB-1 spectra allows us to test this possibility. With a total estimated mass of $20,000 M_{\odot}$ (Currie et al. 2010) Perseus OB-1 comes close to the observed mass range of extragalactic SSCs. We construct a simulated SSC spectrum by adding our observed RSGs weighted by their J -band luminosities. The spectrum is shown in Figure 11. We then apply the same analysis technique as in Section 3 and obtain a metallicity of $Z = -0.03 \pm 0.12$ (NLTE), very similar to the average metallicity obtained from the analysis of the 11 individual spectra. The effective temperature obtained from the cluster spectrum is $T_{\text{eff}} = 3970 \pm 30$ and the gravity $\log g = +0.1 \pm 0.2$. In agreement with the LTE study of the individual Perseus OB-1 supergiants we measured $Z = +0.08 \pm 0.12$, $T_{\text{eff}} = 3910 \pm 70$, and $\log g = +0.2 \pm 0.1$ when fitting with the full LTE model grid.

Gazak et al. (2013) find that the RSG supergiant population will provide $\sim 95\%$ of the J -band flux in a young SSC. To simulate the effect of the 5% contaminative flux we added a flat spectrum of 5% of the total flux. We then re-fit the spectrum and measured -0.08 ± 0.13 (NLTE) and $+0.06 \pm 0.14$ (LTE). The change in measured metallicity is minimal (with a systematic offset of at most $+0.05$ dex) and in the proper direction—contaminant flux will weaken the deepest lines more strongly and thus a drop in extracted metallicity is to be expected. However, the two results agree statistically and offer strong evidence that spectroscopy of unresolved young SSCs can become a powerful application of the J -band technique. We find in this case that an unresolved cluster of proper age can be successfully fit with a single RSG template model, a technique which has been used at very high resolution in the H band (Larsen et al. 2006).

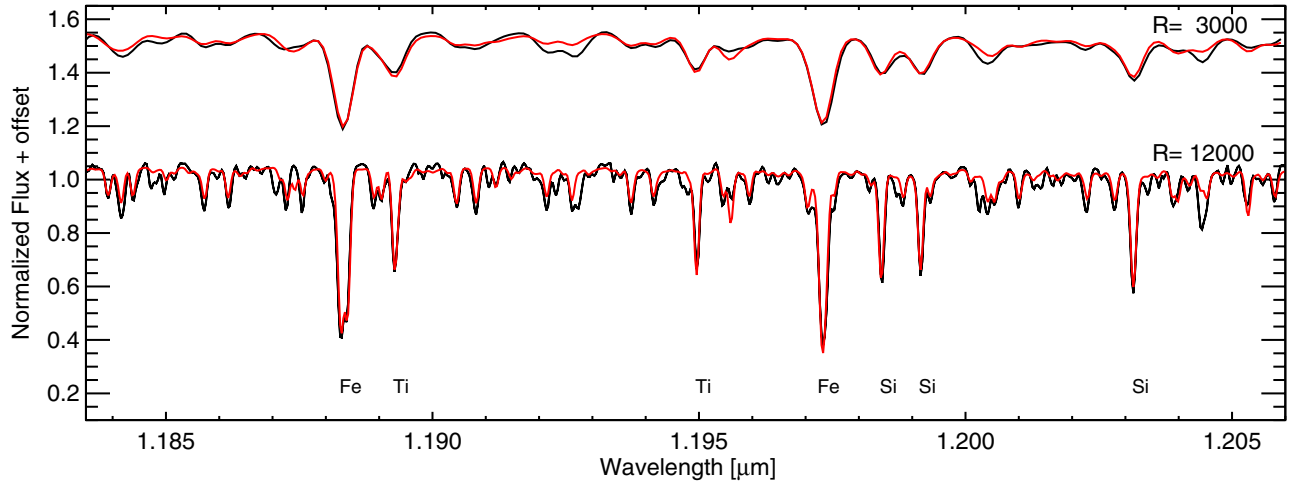


Figure 11. Resulting “cluster spectrum” created when all eleven RSG spectra are summed together as weighted by their J magnitudes. The spectrum is plotted twice, and on the lower spectrum we over plot the best fitting model in red.

(A color version of this figure is available in the online journal.)

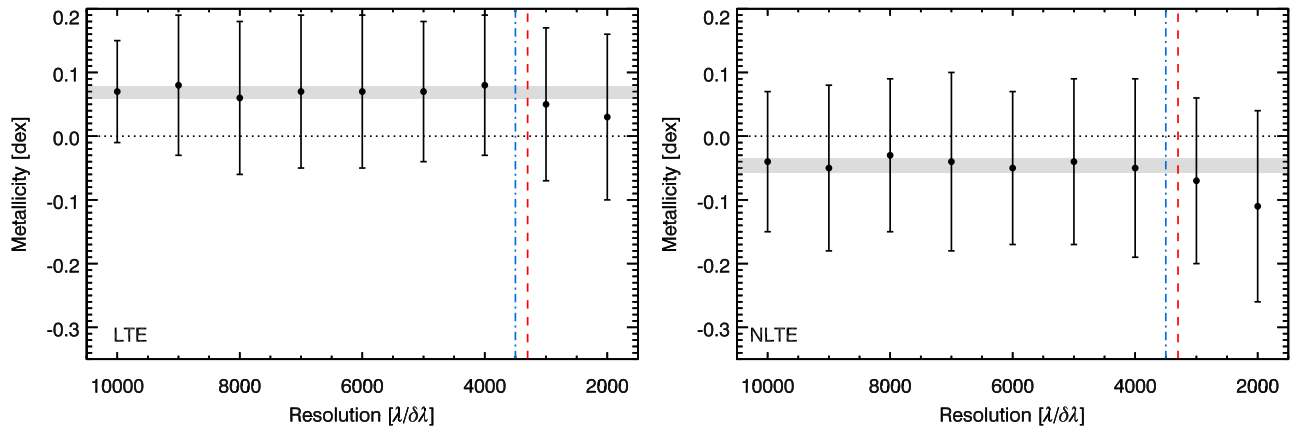


Figure 12. Evolution of the average measured metallicity for our sample of Perseus OB-1 stars collapsed into a synthetic cluster spectrum as a function of spectral resolution. Error bars are derived using the Monte Carlo technique discussed in Section 3.4. The horizontal gray region shows $\pm 1\sigma$ of the average metallicity between $10,000 \leq R \leq 3000$, demonstrating the stability of the technique down to resolutions of $R = 3000$. Vertical lines mark the spectral resolutions of key J -band spectrographs, KMOS on VLT in dash-dotted blue and MOSFIRE on Keck in dashed red. A horizontal dotted line marks solar metallicity. We plot results from the LTE model grid (left panel) and NLTE grid (right panel).

(A color version of this figure is available in the online journal.)

We scale the resolution of our synthetic cluster spectrum down to $R = 2000$. The results of this work echo that of the individual stars, showing stability in fit parameters down to resolutions around 3000. The NLTE and LTE cases of this test are plotted in Figure 12.

6. CONCLUSIONS

In this paper we have tested the J -band technique for extracting metallicity information from modest resolution spectra of RSGs. Through a careful suite of tests we have demonstrated the precision and accuracy of the technique. We obtain reliable abundances in agreement with high resolution, high signal to noise spectroscopy of young massive B-stars in the solar neighborhood. Using the advantage that all of our RSGs formed within a stellar cluster we test our derived parameters against predictions of stellar evolution theory for a cluster of mass and age of Perseus OB-1. Our results are in good agreement with such theoretical work. We thus confirm the technique presented in DFK10 and show that it remains stable down to resolutions

of $R \approx 3000$. This provides a reliable method to determine extragalactic metallicities from individual RSGs to distances of 7–10 Mpc with existing telescopes and instruments. Both Keck (MOSFIRE) and the VLT (KMOS) have multi object spectrographs in the near-IR which operate above resolutions of 3000. With these instruments and the J -band technique, RSGs across the entire disks of star forming galaxies can be observed efficiently.

By utilizing the large populations of RSGs in young, spatially unresolved SSCs we can extend the applicability of the J -band technique out to distances ten times greater with the same instruments. Thus SSCs may allow us to reach beyond the local group and measure the metallicities of star forming galaxies from the stars themselves instead of relying on existing techniques which are empirically calibrated.

We note that low resolution work is now needed in targets expected to be sub solar and super solar in metallicity. The successful application of the J -band technique in such cases would pose the methods tested in this paper to study the metallicity evolution of star forming galaxies in a large volume of the nearby universe.

J.Z.G. and R.P.K. acknowledge support by the National Science Foundation under grant AST-1108906 and the hospitality of the Munich University Observatory where part of this work was carried out. This work was partly supported by the European Union FP7 program through ERC grant number 320360. B.D. is supported by a fellowship from the Royal Astronomical Society. BP is supported in part by the Programme National de Physique Stellaire of the INSU CNRS. We thank our referee, F. Najjarro, for improvements to this manuscript based on his careful review.

REFERENCES

- Alvarez, R., & Plez, B. 1998, *A&A*, **330**, 1109
- Asplund, M., Grevesse, N., Sauval, A. J., & Scott, P. 2009, *ARA&A*, **47**, 481
- Bergemann, M., Kudritzki, R.-P., Plez, B., et al. 2012, *ApJ*, **751**, 156
- Bergemann, M., Kudritzki, R.-P., Würl, M., et al. 2013, *ApJ*, **764**, 115
- Bergemann, M., Ruchti, G., Serenelli, A., et al. 2014, arXiv:1401.4437B
- Bresolin, F., Gieren, W., Kudritzki, R., et al. 2009, *ApJ*, **700**, 309
- Bresolin, F., Pietrzyński, G., Urbaneja, M. A., et al. 2006, *ApJ*, **648**, 1007
- Bresolin, F., Schaerer, D., González Delgado, R. M., & Stasińska, G. 2005, *A&A*, **441**, 981
- Bresolin, F., Urbaneja, M. A., Gieren, W., Pietrzyński, G., & Kudritzki, R. 2007, *ApJ*, **671**, 2028
- Brooks, A. M., Governato, F., Booth, C. M., et al. 2007, *ApJL*, **655**, L17
- Cardelli, J. A., Clayton, G. C., & Mathis, J. S. 1989, *ApJ*, **345**, 245
- Chiavassa, A., Freytag, B., Masseron, T., & Plez, B. 2011, *A&A*, **535**, A22
- Colavitti, E., Matteucci, F., & Murante, G. 2008, *A&A*, **483**, 401
- Cunha, K., Sellgren, K., Smith, V. V., et al. 2007, *ApJ*, **669**, 1011
- Currie, T., Hernandez, J., Irwin, J., et al. 2010, *ApJS*, **186**, 191
- Davies, B., Kudritzki, R., & Figuer, D. F. 2010, *MNRAS*, **407**, 1203
- Davies, B., Kudritzki, R.-P., Plez, B., et al. 2013, *ApJ*, **767**, 3
- De Lucia, G., Kauffmann, G., & White, S. D. M. 2004, *MNRAS*, **349**, 1101
- de Rossi, M. E., Tissera, P. B., & Scannapieco, C. 2007, *MNRAS*, **374**, 323
- Ercolano, B., Wesson, R., & Bastian, N. 2010, *MNRAS*, **401**, 1375
- Evans, C. J., Bresolin, F., Urbaneja, M. A., et al. 2007, *ApJ*, **659**, 1198
- Evans, C. J., Davies, B., Kudritzki, R.-P., et al. 2011, *A&A*, **527**, A50
- Finlator, K., & Davé, R. 2008, *MNRAS*, **385**, 2181
- Firnstein, M., & Przybilla, N. 2012, *A&A*, **543**, A80
- Garmany, C. D., & Stencel, R. E. 1992, *A&AS*, **94**, 211
- Garnett, D. R. 2004, in *Cosmochemistry: The Melting Pot of the Elements*, ed. C. Esteban, R. García López, A. Herrero, & F. Sánchez (Cambridge: Cambridge Univ. Press), 171
- Gazak, J. Z., Bastian, N., Kudritzki, R.-P., et al. 2013, *MNRAS*, **430**, L35
- Gustafsson, B., Edvardsson, B., Eriksson, K., et al. 2008, *A&A*, **486**, 951
- Humphreys, R. M., & Davidson, K. 1979, *ApJ*, **232**, 409
- Kewley, L. J., & Ellison, S. L. 2008, *ApJ*, **681**, 1183
- Kobayashi, N., Tokunaga, A. T., Terada, H., et al. 2000, *Proc. SPIE*, **4008**, 1056
- Köppen, J., Weidner, C., & Kroupa, P. 2007, *MNRAS*, **375**, 673
- Kudritzki, R., Urbaneja, M. A., Bresolin, F., et al. 2008, *ApJ*, **681**, 269
- Kudritzki, R.-P., Urbaneja, M. A., Gazak, Z., et al. 2012, *ApJ*, **747**, 15
- Larsen, S. S., Origlia, L., Brodie, J. P., & Gallagher, J. S. 2006, *MNRAS*, **368**, L10
- Lequeux, J., Peimbert, M., Rayo, J. F., Serrano, A., & Torres-Peimbert, S. 1979, *A&A*, **80**, 155
- Levesque, E. M., Massey, P., Olsen, K. A. G., et al. 2005, *ApJ*, **628**, 973
- Lundqvist, M., & Wahlgren, G. M. 2005, *NuPhA*, **758**, 304
- Maiolino, R., Nagao, T., Grazian, A., et al. 2008, *A&A*, **488**, 463
- Meynet, G., & Maeder, A. 2000, *A&A*, **361**, 101
- Nieva, M.-F., & Przybilla, N. 2012, *A&A*, **539**, A143
- Plez, B. 2012, *Turbospectrum: Code for Spectral Synthesis*, Astrophysics Source Code Library, 1205.004
- Prantzos, N., & Boissier, S. 2000, *MNRAS*, **313**, 338
- Ramírez, S. V., Sellgren, K., Carr, J. S., et al. 2000, *ApJ*, **537**, 205
- Sánchez-Blázquez, P., Courty, S., Gibson, B. K., & Brook, C. B. 2009, *MNRAS*, **398**, 591
- Skrutskie, M. F., Cutri, R. M., Stiening, R., et al. 2006, *AJ*, **131**, 1163
- Stasińska, G. 2005, *A&A*, **434**, 507
- Tremonti, C. A., Heckman, T. M., Kauffmann, G., et al. 2004, *ApJ*, **613**, 898
- U, V., Urbaneja, M. A., Kudritzki, R., et al. 2009, *ApJ*, **704**, 1120
- Urbaneja, M. A., Kudritzki, R., Bresolin, F., et al. 2008, *ApJ*, **684**, 118
- Wahlgren, G. M., Nave, G., Nilsson, H., & Lundqvist, M. 2008, *JPhCS*, **130**, 012019
- Wiersma, R. P. C., Schaye, J., Theuns, T., Dalla Vecchia, C., & Tornatore, L. 2009, *MNRAS*, **399**, 574
- Yin, J., Hou, J. L., Prantzos, N., et al. 2009, *A&A*, **505**, 497
- Zurita, A., & Bresolin, F. 2012, *MNRAS*, **427**, 1463